Reconstruction of Enhanced Ultrasound Images From Compressed Measurements Using Simultaneous Direction Method of Multipliers

Zhouye Chen, Adrian Basarab, Denis Kouamé

Reconstruction of Enhanced Ultrasound Images From Compressed Measurements Using Simultaneous Direction Method of Multipliers

Zhouye Chen, *Student Member, IEEE*, Adrian Basarab, *Member, IEEE*, and Denis Kouamé, *Member, IEEE*

***Abstract*— High-resolution ultrasound (US) image reconstruction from a reduced number of measurements is of great interest in US imaging, since it could enhance both frame rate and image resolution. Compressive deconvolution (CD), combining compressed sensing and image deconvolution, represents an interesting possibility to consider this challenging task. The model of CD includes, in addition to the compressive sampling matrix, a 2-D convolution operator carrying the information on the system point spread function. Through this model, the resolution of reconstructed US images from compressed measurements mainly depends on three aspects: the acquisition setup, i.e., the incoherence of the sampling matrix, the image regularization, i.e., the sparsity prior, and the optimization technique. In this paper, we mainly focused on the last two aspects. We proposed a novel simultaneous direction method of multipliers based optimization scheme to invert the linear model, including two regularization terms expressing the sparsity of the RF images in a given basis and the generalized Gaussian statistical assumption on tissue reflectivity functions. The performance of the method is evaluated on both simulated and *in vivo* data.**

***Index Terms*— Compressive deconvolution (CD), simultaneous direction method of multipliers (SDMM), ultrasound (US) imaging.**

I. Introduction

SINCE the applicability of compressive sampling (CS) to 2-D and 3-D Ultrasound (US) imaging (see [2]–[9]) or to duplex Doppler [10] has been proved, the topic of CS in the field of US imaging attracted a growing interest from several research groups. CS is a mathematical framework allowing to recover a compressible image, via nonlinear optimization routines, from a few linear measurements (below the limit standardly imposed by the Shannon–Nyquist theorem) [11], [12]. According to the CS theory, this reconstruction is possible provided that the restricted isometry property (RIP), characterizing the measurement matrix, holds [11], [12]. The RIP has been extensively explored in the literature for several classes of matrices. The most common examples that guarantee the respect of RIP for a number of measurements linearly depending on the sparsity level of the image to recover include random Gaussian or Bernoulli matrices or the partial Fourier matrix.

The main objective of CS application in US imaging systems, as highlighted by the existing works, is to increase the frame rate and/or to decrease the amount of acquired data and/or to decrease the computational complexity of beamforming [3], [4], [8]. Despite the promising results, the application of CS in US imaging still remains challenging, with issues related to the appropriate acquisition schemes, the sparsifying transforms, and the reconstruction algorithms that represent the main objective of this paper. We may remark that the RIP cannot strictly hold in practical situations, mainly because of the lack of incoherence between the practical measurement and sparsity basis or because of the low level of sparsity of US images. As a consequence, the images reconstructed through CS are usually less good compared with those reconstructed through standard acquisitions, especially when the CS ratio (CS ratio) is low. In this paper, the CS ratio refers to the ratio between the number of linear measurements and the number of samples in the image to reconstruct. Second, the resolution of the reconstructed images is equivalent to those acquired using standard schemes at most. Nonetheless, it is well known that the spatial resolution, the signal-to-noise ratio (SNR), and the contrast of standard US images are affected by the limited bandwidth of the imaging transducer, the physical phenomena related to US wave propagation such as diffraction, and the imaging system.

In order to overcome these issues, we have recently proposed a compressive deconvolution (CD) method aiming to reconstruct enhanced RF images from compressed linear measurements [13]. The main idea behind CD is to combine CS and deconvolution reconstructions into a unique framework leading to the following linear model:

$$\boldsymbol{y} = \Phi H \boldsymbol{x} + \boldsymbol{n} \tag{1}$$

where $\boldsymbol{y} \in \mathbb{R}^M$ contains M linear measurements obtained by projecting one RF image $H\boldsymbol{x} \in \mathbb{R}^N$ onto the CS acquisition matrix $\Phi \in \mathbb{R}^{M \times N}$, with $M \ll N$. $H \in \mathbb{R}^{N \times N}$ is a block circulant with circulant block matrix modeling the 2-D convolution between the 2-D point spread function (PSF)

Manuscript received April 19, 2016; accepted July 20, 2016. Date of publication July 21, 2016; date of current version October 1, 2016. The work was supported in part by ANR-11-LABX-0040-CIMI within the program ANR-11-IDEX-0002-02 of the University of Toulouse and CSC (Chinese Scholarship Council). This paper was presented at the IEEE International Ultrasonics Symposium 2015 conference [1].

The authors are with the Centre National de la Recherche Scientifique, Institut de Recherche en Informatique de Toulouse, University of Toulouse, Toulouse 31062, France (e-mail: zhouye.chen@irit.fr; basarab@irit.fr; kouame@irit.fr).

Digital Object Identifier 10.1109/TUFFC.2016.2593795

of the US system and the tissue reflectivity function (TRF) $\boldsymbol{x} \in \mathbb{R}^N$. In other words, the multiplication of the TRF by H models the US RF image degradation mentioned above. Finally, $\boldsymbol{n} \in \mathbb{R}^M$ stands for a zero-mean additive white Gaussian noise. We emphasize that all the images in (1) are expressed in the standard lexicographical order.

We should note that similar models have been recently proposed for general image processing purpose [14]–[18] including a theoretical derivation of RIP for random mask imaging [19]. Nevertheless, in contrast to the solutions provided by these existing works, we showed in [13] that inverting (1) by minimizing the following unconstrained objective function is well suitable for US imaging:

$$\hat{\boldsymbol{x}} = \underset{x}{\operatorname{argmin}} \|\Psi^{-1} H\boldsymbol{x}\|_1 + \alpha\|\boldsymbol{x}\|_p^p + \frac{1}{2\mu}\|\boldsymbol{y} - \Phi H\boldsymbol{x}\|_2^2. \tag{2}$$

This objective function is composed of three terms.

1) The l_1-norm term that aims at imposing the sparsity of the RF data $H\boldsymbol{x}$ in a transformed domain Ψ.
2) The l_p-norm ($1 \leq p \leq 2$) regularizing the TRF $\boldsymbol{x}$ based on the generalized Gaussian distribution (GGD) statistical assumption of US images (p is related to the shape parameter of the GGD) (see [20]–[22]).
3) The data fidelity term. In order to solve the optimization problem in (2), the solution proposed in [13] was based on the alternative direction method of multipliers (ADMM) [23].

In this paper, we further improve the US CD scheme in [13] by proposing a new reconstruction algorithm based on the simultaneous direction method of multipliers (SDMM) [24]. The results on simulated and experimental images show improved convergence properties obtained with the proposed optimization routine, resulting in at least equivalent reconstruction results and lower computational times compared with our previous work. Moreover, we extend the CD approach to nonorthogonal measurement matrices, thus covering a more general compressed acquisition model.

This paper is organized as follows. We first recall the general framework of SDMM in Section II. The proposed SDMM-based optimization scheme able to solve (2) is detailed in Section III. In Section IV, the simulated and experimental results are provided to show the effectiveness of the proposed method and its efficiency in recovering the TRF from compressed US data. Conclusions are drawn in Section V.

II. General Framework of Simultaneous Direction Method of Multipliers

The algorithm of SDMM [24] generalizes the alternating split Bregman (ASB) method [25] to a sum of more than two functions. The ASB was initially proposed to solve optimization problems that can be expressed in the following form:

$$\underset{u\in\mathbb{R}^s, v\in\mathbb{R}^t}{\operatorname{argmin}} \; f(u) + g(v) \quad s.t.\; v = Cu \tag{3}$$

where $C \in \mathbb{R}^{t\times s}$ is a given matrix and $f : \mathbb{R}^s \to \bar{\mathbb{R}}$ and $g : \mathbb{R}^t \to \bar{\mathbb{R}}$ are convex functions. $\bar{\mathbb{R}}$ is designated for extended real numbers, i.e., $\mathbb{R} \bigcup \{+\infty\}$.

The iterative ASB method declines as follows:

$$u^{k+1} = \underset{u\in\mathbb{R}^s}{\operatorname{argmin}} f(u) + \frac{1}{2\beta}\|b^k + Cu - v^k\|_2^2 \tag{4}$$

$$v^{k+1} = \underset{v\in\mathbb{R}^t}{\operatorname{argmin}} g(v) + \frac{1}{2\beta}\|b^k + Cu^{k+1} - v\|_2^2 \tag{5}$$

$$b^{k+1} = b^k + Cu^{k+1} - v^{k+1} \tag{6}$$

where $b \in \mathbb{R}^t$ is the Lagrangian parameter. It has been proved that the ASB method is equivalent to ADMM when the constraints are linear [26].

Inspired from ASB, the general optimization problem considered in the framework of SDMM is

$$\underset{u\in\mathbb{R}^s}{\operatorname{argmin}} \sum_{i=1}^{m} f_i(C_i u) \tag{7}$$

where $C_i \in \mathbb{R}^{t_i,s}$ and $f_i : \mathbb{R}^{t_i} \to \bar{\mathbb{R}}$ are convex functions. Considering $v_i \in \mathbb{R}^{t_i}$, $v_i = C_i u$, $f(u) = \langle 0, u\rangle$, and $g(v) = \sum_{i=1}^m f_i(v_i)$, (7) can be reformulated as

$$\underset{u\in\mathbb{R}^s, v_i\in\mathbb{R}_i^t}{\operatorname{argmin}} \; f(u) + \sum_{i=1}^{m} f_i(v_i). \tag{8}$$

Similar to the ASB method, SDMM iteratively solves the above optimization problem as follows:

$$u^{k+1} = \underset{u\in\mathbb{R}^s}{\operatorname{argmin}} \frac{1}{2\beta}\left\| \begin{pmatrix} b_1^k \\ \vdots \\ b_m^k \end{pmatrix} + \begin{pmatrix} C_1 \\ \vdots \\ C_m \end{pmatrix} u - \begin{pmatrix} v_1^k \\ \vdots \\ v_m^k \end{pmatrix} \right\|^2 \tag{9}$$

$$\begin{pmatrix} v_1^{k+1} \\ \vdots \\ v_m^{k+1} \end{pmatrix} = \underset{v_i\in\mathbb{R}_i^t}{\operatorname{argmin}} \left\{ \frac{1}{2\beta}\left\| \begin{pmatrix} b_1^k \\ \vdots \\ b_m^k \end{pmatrix} + \begin{pmatrix} C_1 \\ \vdots \\ C_m \end{pmatrix} u^{k+1} - \begin{pmatrix} v_1 \\ \vdots \\ v_m \end{pmatrix} \right\|^2 + \sum_{i=1}^{m} f_i(v_i) \right\} \tag{10}$$

$$\begin{pmatrix} b_1^{k+1} \\ \vdots \\ b_m^{k+1} \end{pmatrix} = \begin{pmatrix} b_1^k \\ \vdots \\ b_m^k \end{pmatrix} + \begin{pmatrix} C_1 \\ \vdots \\ C_m \end{pmatrix} u^{k+1} - \begin{pmatrix} v_1^{k+1} \\ \vdots \\ v_m^{k+1} \end{pmatrix}. \tag{11}$$

III. Proposed Compressive Deconvolution Method

In this paper, we propose an SDMM-based optimization scheme adapted to solve the problem in (2). First, we remark that (2) can be reformulated as

$$\underset{\boldsymbol{x}}{\operatorname{argmin}} \; f_1(\boldsymbol{v}_1) + f_2(\boldsymbol{v}_2) + f_3(\boldsymbol{v}_3) \tag{12}$$

with

$$\begin{cases} f_1(\boldsymbol{v}_1) = \alpha\|\boldsymbol{v}_1\|_p^p \\ f_2(\boldsymbol{v}_2) = \|\boldsymbol{v}_2\|_1 \\ f_3(\boldsymbol{v}_3) = \dfrac{1}{2\mu}\|\boldsymbol{y} - \Phi\boldsymbol{v}_3\|_2^2 \\ \boldsymbol{v}_1 = C_1\boldsymbol{x}, \quad \boldsymbol{v}_2 = C_2\boldsymbol{x}, \; \boldsymbol{v}_3 = C_3\boldsymbol{x} \\ C_1 = I_N, \quad C_2 = \Psi^{-1}H, \; C_3 = H. \end{cases}$$

Using the above parametrization, the SDMM steps given in (9)–(11) write for our CD problem as follows:

$$\boldsymbol{x}^{k+1} = \underset{\boldsymbol{x}\in\mathbb{R}^N}{\operatorname{argmin}} \frac{1}{2\beta} \left\| \begin{pmatrix} \boldsymbol{b}_1^k \\ \boldsymbol{b}_2^k \\ \boldsymbol{b}_3^k \end{pmatrix} + \begin{pmatrix} I_N \\ \Psi^{-1}H \\ H \end{pmatrix} \boldsymbol{x} - \begin{pmatrix} \boldsymbol{v}_1^k \\ \boldsymbol{v}_2^k \\ \boldsymbol{v}_3^k \end{pmatrix} \right\|^2 \tag{13}$$

$$\begin{pmatrix} \boldsymbol{v}_1^{k+1} \\ \boldsymbol{v}_2^{k+1} \\ \boldsymbol{v}_3^{k+1} \end{pmatrix} = \underset{\boldsymbol{v}_1,\boldsymbol{v}_2,\boldsymbol{v}_3}{\operatorname{argmin}} \left\{ \frac{1}{2\beta} \left\| \begin{pmatrix} \boldsymbol{b}_1^k \\ \boldsymbol{b}_2^k \\ \boldsymbol{b}_3^k \end{pmatrix} + \begin{pmatrix} I_N \\ \Psi^{-1}H \\ H \end{pmatrix} \boldsymbol{x}^{k+1} - \begin{pmatrix} \boldsymbol{v}_1 \\ \boldsymbol{v}_2 \\ \boldsymbol{v}_3 \end{pmatrix} \right\|^2 + \sum_{i=1}^{3} f_i(\boldsymbol{v}_i) \right\} \tag{14}$$

$$\begin{pmatrix} \boldsymbol{b}_1^{k+1} \\ \boldsymbol{b}_2^{k+1} \\ \boldsymbol{b}_3^{k+1} \end{pmatrix} = \begin{pmatrix} \boldsymbol{b}_1^k \\ \boldsymbol{b}_2^k \\ \boldsymbol{b}_3^k \end{pmatrix} + \begin{pmatrix} I_N \\ \Psi^{-1}H \\ H \end{pmatrix} \boldsymbol{x}^{k+1} - \begin{pmatrix} \boldsymbol{v}_1^{k+1} \\ \boldsymbol{v}_2^{k+1} \\ \boldsymbol{v}_3^{k+1} \end{pmatrix}. \tag{15}$$

In the following, we give the details of solving each of the above steps. First, we remark that (13) is a classical l_2-norm minimization problem that can be efficiently solved in the Fourier domain [27].

Equation (14) consists in solving three subproblems, corresponding to the update of $\boldsymbol{v}_1$, $\boldsymbol{v}_2$, and $\boldsymbol{v}_3$, respectively. The $\boldsymbol{v}_1$-subproblem can be solved as follows:

$$\begin{aligned} \boldsymbol{v}_1^{k+1} &= \underset{\boldsymbol{v}_1}{\operatorname{argmin}} \alpha \|\boldsymbol{v}_1\|_p^p + \frac{1}{2\beta} \left\| \boldsymbol{b}_1^k + \boldsymbol{x}^{k+1} - \boldsymbol{v}_1 \right\|_2^2 \\ &= \operatorname{prox}_{\alpha\beta\|\cdot\|_p^p} \left(\boldsymbol{b}_1^k + \boldsymbol{x}^{k+1} \right) \end{aligned} \tag{16}$$

where prox represents the proximal operator [28]–[30]. The proximal operator of $\|\boldsymbol{x}\|_p^p$ has been given explicitly in [31] and used in [32]. More details about the proximal operator can be found in Appendix A.

The $\boldsymbol{v}_2$-subproblem can also be solved using the proximal operator associated with the ℓ_1-norm that corresponds to the soft thresholding operator [27] (see Appendix A)

$$\begin{aligned} \boldsymbol{v}_2^{k+1} &= \underset{\boldsymbol{v}_2}{\operatorname{argmin}} \|\boldsymbol{v}_2\|_1 + \frac{1}{2\beta} \left\| \boldsymbol{b}_2^k + \Psi^{-1}H\boldsymbol{x}^{k+1} - \boldsymbol{v}_2 \right\|_2^2 \\ &= \operatorname{prox}_{\beta\|\cdot\|_1} \left(\boldsymbol{b}_2^k + \Psi^{-1}H\boldsymbol{x}^{k+1} \right). \end{aligned} \tag{17}$$

Finally, the $\boldsymbol{v}_3$-subproblem can be solved as follows:

$$\begin{aligned} \boldsymbol{v}_3^{k+1} &= \underset{\boldsymbol{v}_3}{\operatorname{argmin}} \frac{1}{2\mu} \|y - \Phi\boldsymbol{v}_3\|_2^2 + \frac{1}{2\beta} \left\| \boldsymbol{b}_3^k + H\boldsymbol{x}^{k+1} - \boldsymbol{v}_3 \right\|_2^2 \\ &\Leftrightarrow [\beta\Phi^t\Phi + \mu]\boldsymbol{v}_3^{k+1} = \beta\Phi^t\boldsymbol{y} + \mu\boldsymbol{b}_3^k + \mu H\boldsymbol{x}^{k+1}. \end{aligned} \tag{18}$$

For orthogonal sampling matrices Φ, the Sherman–Morrison–Woodbury inversion matrix lemma [33] allows us to efficiently find the solution of the above $\boldsymbol{v}_3$-subproblem [32]. However, when the sampling matrix Φ is nonorthogonal, the solution of $\boldsymbol{v}_3$-subproblem in (18) cannot be computed in practical situations because of the high-dimensional matrices. To overcome this issue and make our CD method more general and therefore relevant to various compressive acquisition schemes in US imaging, we propose to use Newton's method to approximate its solution.

Let us denote

$$h(\boldsymbol{v}_3) = [\beta\Phi^t\Phi + \mu]\boldsymbol{v}_3 - \beta\Phi^t\boldsymbol{y} + \mu\boldsymbol{b}_3^k + \mu H\boldsymbol{x}^{k+1}. \tag{19}$$

At each iteration, we approximate $\boldsymbol{v}_3^{k+1}$ by

$$\boldsymbol{v}_3^{k+1} = \boldsymbol{v}_3^k - \text{stp} * h\left(\boldsymbol{v}_3^k\right) \tag{20}$$

where stp is defined as

$$\text{stp} = \frac{h\left(\boldsymbol{v}_3^k\right)^t h\left(\boldsymbol{v}_3^k\right)}{\beta\left[\Phi h\left(\boldsymbol{v}_3^k\right)\right]^t\left[\Phi h\left(\boldsymbol{v}_3^k\right)\right] + \mu h\left(\boldsymbol{v}_3^k\right)^t h\left(\boldsymbol{v}_3^k\right)}. \tag{21}$$

To conclude, Algorithm 1 summarizes the SDMM-based numerical scheme proposed for solving (2).

Algorithm 1 CD SDMM-Based Algorithm

Input: α, μ, β, $\boldsymbol{v}_i^0$, $\boldsymbol{b}_i^0$, $i = 1, 2, 3$

while not converged **do**
  $\boldsymbol{x}^{k+1} \leftarrow \boldsymbol{v}_i^k, \boldsymbol{b}_i^k$ ▷ update $\boldsymbol{x}^{k+1}$ using (13)
  $\boldsymbol{v}_1^{k+1} \leftarrow \boldsymbol{b}_1^k, \boldsymbol{x}^{k+1}$ ▷ update $\boldsymbol{v}_1^{k+1}$ using (16)
  $\boldsymbol{v}_2^{k+1} \leftarrow \boldsymbol{b}_2^k, \boldsymbol{x}^{k+1}$ ▷ update $\boldsymbol{v}_2^{k+1}$ using (17)
  $\boldsymbol{v}_3^{k+1} \leftarrow \boldsymbol{b}_3^k, \boldsymbol{x}^{k+1}$ ▷ update $\boldsymbol{v}_3^{k+1}$ using (18)
  if Φ is orthogonal **then**
    Solve eq.(18) by Sherman-Morrison-Woodbury inversion matrix lemma
  else
    Solve eq.(18) by using eq.(20)
  end if
  $\boldsymbol{b}_i^{k+1} \leftarrow \boldsymbol{v}_i^{k+1}, \boldsymbol{x}^{k+1}$ ▷ update $\boldsymbol{b}_i^{k+1}$ using (15)
end while

Output: $\boldsymbol{x}$

We emphasize that compared to the ADMM-based scheme that we have recently proposed to solve (2) [13], the method resumed in Algorithm 1 requires one less hyperparameter. Moreover, with the proposed optimization scheme, all the subproblems are solved exactly, while in [13], we have only obtained an approximation for the $\boldsymbol{v}_1$-subproblem in (16). This improvement allows the SDMM-based iterative scheme to converge faster than the ADMM-based algorithm proposed in [13]. Since this $\boldsymbol{v}_1$-subproblem is critical for the deconvolution process, one may also expect more accurate CD results with SDMM than with ADMM.

IV. Simulation Results

In this section, we provide numerical experiments to evaluate the effectiveness of the proposed CD optimization framework, denoted by SDMM hereafter. Since we have recently shown in [13] the superiority of the ADMM-based method (denoted by ADMM in this section) compared with other CD methods, the technique in [13] is used herein for comparison purpose.[1] Finally, a comparison between the proposed method used only for deconvolution purpose, i.e., the measurements represent 100% of the data, and three existing techniques is shown in Appendix B.

[1]The code corresponding to the ADMM-based method is available at http://www.irit.fr/~Adrian.Basarab/codes.html.

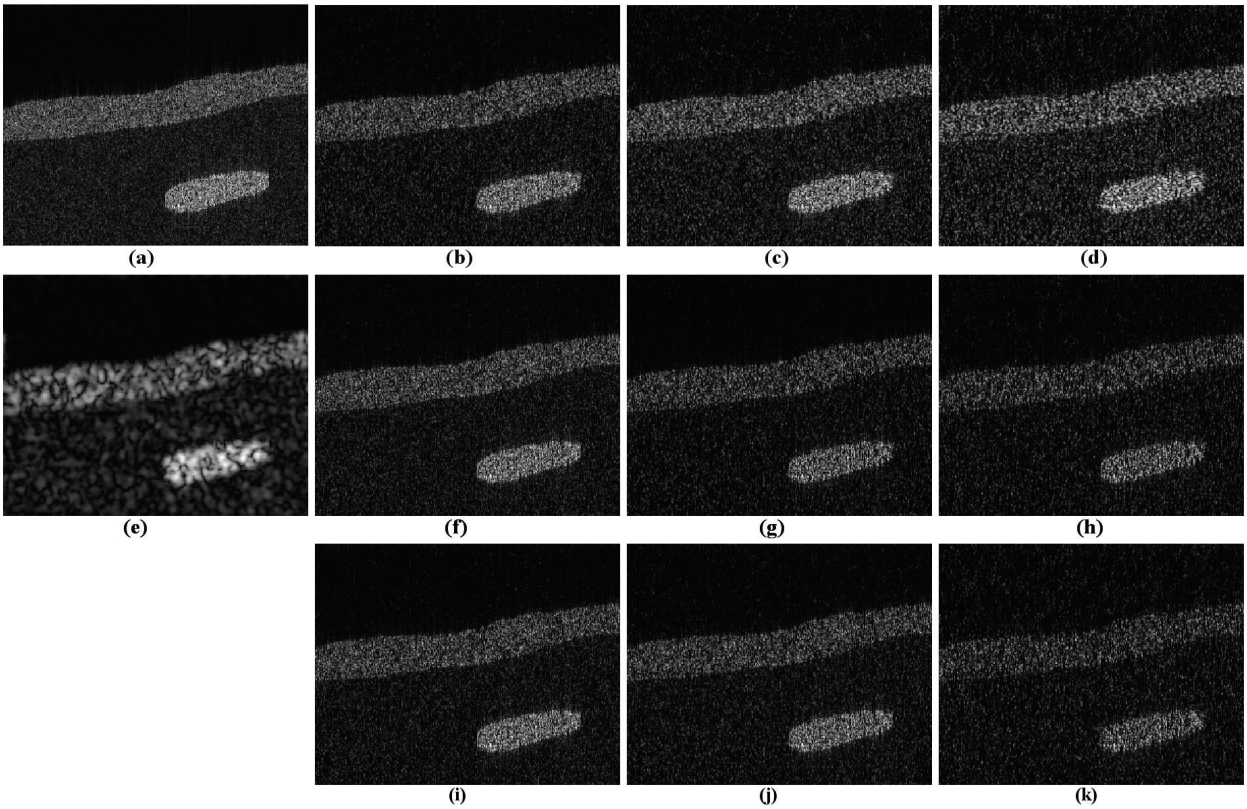

Fig. 1. Results on simulated data (Group 1). (a) TRF. (b)–(d) Reconstruction results using ADMM for CS ratios of 0.6, 0.4, and 0.2. (e) Simulated US image. (f)–(h) Reconstruction results using SDMM for CS ratios of 0.6, 0.4, and 0.2. (i)–(k) Reconstruction results using nSDMM for CS ratios of 0.6, 0.4, and 0.2.

A. Results on Simulated Data

Two groups of simulation experiments (named Group 1 and 2) have been conducted to evaluate the performance of the proposed scheme. The RF images have been generated following the procedure in [34] using a 2-D convolution between a US PSF and a map of scatterers, i.e., TRF.

1) Cartoon Phantom Image: For Group 1, the TRF was generated by assigning the scatterers random amplitudes following a given distribution, weighted by a cartoon image denoted by mask hereafter. A Laplacian distribution has been employed and the mask has been hand drawn to simulate four different regions with different echogenicities. The PSF was generated using a Field II [35] simulation corresponding to a 128-element linear probe operating at 3.5 MHz and an axial sampling frequency of 20 MHz. The resulting TRF and US image (plotted in B-mode) are shown in Fig. 1(a) and (e), respectively. The compressed measurements were obtained by projecting the RF images onto an orthogonal structurally random matrix (SRM) [36] and were degraded by an additive Gaussian noise corresponding to an SNR of 40 dB. In order to evaluate the performance of the algorithm with a nonorthogonal measurement matrix, namely, nSDMM, we have also projected the RF data onto a random Gaussian matrix. The corresponding results are provided in Fig. 1(i)–(k).

2) Simulated Kidney Image: The PSF for Group 2 was also generated with Field II [35] and corresponds to a sectorial probe with the central frequency of 4 MHz and an axial sampling frequency of 40 MHz. The TRF follows one of the examples proposed by the Field II simulator [34], mimicking a kidney. The sampling matrix considered was an SRM [36] and the SNR was set at 40 dB. The TRF and the simulated US image are displayed in Fig. 2(a) and (e), respectively.

3) Discussion of the Results: Figs. 1 and 2 display the CD reconstruction results obtained with different methods for CS ratios of 0.6, 0.4, and 0.2. The value of p used to regularize the TRF estimations was set to 1 for Group 1 and 1.5 for Group 2. All the other hyperparameters were manually set to their best possible values by cross validation. We should note that since both ADMM and SDMM methods aim at solving the same objective function in (2), the hyperparameters α and μ have been assigned the same values in order to ensure a fair comparison. For the same reason, both algorithms were assigned the same convegence criterion, i.e., $\|\boldsymbol{x}^k - \boldsymbol{x}^{k-1}\|/\|\boldsymbol{x}^{k-1}\| < 5e^{-4}$, with k the iteration number and $\boldsymbol{x}_k$ the estimated image at iteration k.

Taking benefit from the fact that the TRF ground truth is available in simulation experiments, the peak SNR (PSNR) and the structural similarity (SSIM) are used in this paper to assess the quality of the reconstruction results. A higher PSNR or SSIM indicates that the reconstruction is of higher quality. PSNR is usually expressed in terms of the logarithmic decibel scale and defined as

$$\text{PSNR} = 10\log_{10}\frac{NL^2}{\boldsymbol{x} - \hat{\boldsymbol{x}}} \tag{22}$$

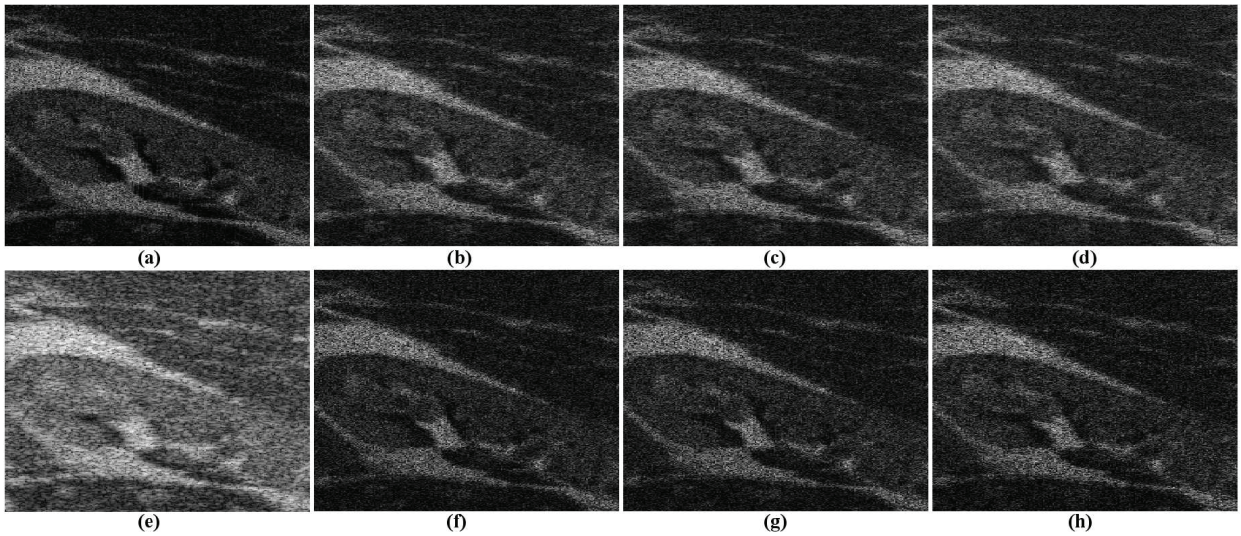

Fig. 2. Results on simulated data (Group 2). (a) TRF. (b)–(d) Reconstruction results using ADMM for CS ratios of 0.6, 0.4, and 0.2. (e) Simulated US image. (f)–(h) Reconstruction results using SDMM for CS ratios of 0.6, 0.4, and 0.2.

where $\boldsymbol{x}$ and $\hat{\boldsymbol{x}}$ are the original and reconstructed images, respectively, and the constant L represents the maximum intensity value in $\boldsymbol{x}$. SSIM is usually measured in percentage and defined as

$$\text{SSIM} = \frac{(2\mu_{\boldsymbol{x}}\mu_{\hat{\boldsymbol{x}}} + c_1)(2\sigma_{\boldsymbol{x}\hat{\boldsymbol{x}}} + c_2)}{\left(\mu_{\boldsymbol{x}}^2 + \mu_{\hat{\boldsymbol{x}}}^2 + c_1\right)\left(\sigma_{\boldsymbol{x}}^2 + \sigma_{\hat{\boldsymbol{x}}}^2 + c_2\right)} \tag{23}$$

where $\boldsymbol{x}$ and $\hat{\boldsymbol{x}}$ are the original and reconstructed images, respectively, $\mu_{\boldsymbol{x}}$ and $\mu_{\hat{\boldsymbol{x}}}$ and $\sigma_{\boldsymbol{x}}$ and $\sigma_{\hat{\boldsymbol{x}}}$ are the mean and variance values of $\boldsymbol{x}$ and $\hat{\boldsymbol{x}}$, respectively, $\sigma_{\boldsymbol{x}\hat{\boldsymbol{x}}}$ is the covariance between $\boldsymbol{x}$ and $\hat{\boldsymbol{x}}$, and $c_1 = (k_1 C)^2$ and $c_2 = (k_2 C)^2$ are two variables aiming at stabilizing the division with weak denominator, C is the dynamic range of the pixel-values, and k_1 and k_2 are constants. Herein, $C = 1$, $k_1 = 0.01$, and $k_2 = 0.03$.

These quantitative results are regrouped in Table I, where the reported PSNRs and SSIMs are the mean values of ten experiments. The bold values stand for the best result obtained for each experiment. Note that given the more complex structures in Group 2, the intrinsic values of PSNR and SSIM are lower for Group 2 than for Group 1. However, the improvement between SDMM and ADMM is globally higher for Group 2 than for Group 1.

Both the visual inspection of images in Figs. 1 and 2 and the quantitative results in Table I show that the proposed SDMM-based method outperforms the ADMM algorithm for the two simulated images and all the CS ratios. In addition to the reconstruction quality gain, the proposed method also offers better convergence properties compared with ADMM. This convergence improvement is clearly highlighted by the plots in Fig. 3. We may thus remark that for all the CS ratios, the convergence curves, both in terms of objective function [as (2)] and normalized mean square error (NMSE) defined in (24), decrease much faster with SDMM than with ADMM. The computations were performed using a computer with Intel Xeon CPU E5620 @2.40 GHz, 4.00-GB RAM.

TABLE I

QUANTITATIVE RESULTS FOR CD RECONSTRUCTION OF SIMULATED US IMAGES

	CS ratios	0.8	0.6	0.4	0.2
Group 1					
ADMM	PSNR(dB)	29.14	28.34	27.01	24.60
	SSIM(%)	81.58	77.44	69.07	51.65
SDMM	PSNR(dB)	**30.67**	**29.55**	**27.94**	**26.18**
	SSIM(%)	**85.77**	**81.66**	**74.37**	**63.15**
Group 2					
ADMM	PSNR(dB)	28.02	26.89	26.20	25.32
	SSIM(%)	60.56	58.20	54.21	45.35
SDMM	PSNR(dB)	**31.53**	**30.95**	**30.19**	**28.10**
	SSIM(%)	**76.85**	**74.45**	**70.40**	**56.20**

Depending on the stopping criterion, the convergence rate of SDMM for Group 1 is at least twice faster than the one of ADMM. We emphasize that the same convergence properties have been obtained for Group 2. The convergence performance of nSDMM is also shown in Fig. 3. We may remark that nSDMM has degraded convergence properties compared with the SDMM method, caused by the approximation in (20). However, when the convergence is achieved, both the objective function value and the NMSE obtained with nSDMM and SDMM are similar

$$\text{NMSE} = \frac{1}{N}\|\boldsymbol{x} - \hat{\boldsymbol{x}}\|_2^2 \tag{24}$$

where $\boldsymbol{x}$ and $\hat{\boldsymbol{x}}$ are the normalized original and reconstructed TRF images, respectively, and N represents the number of pixels in the image.

As explained previously, the value of the regularization parameter p has been manually tuned in the two simulated experiments. However, one may observe the importance of this parameter on the reconstruction results, as it directly affects the regularization of the TRF [22]. In order to show its influence on the results, we regroup in Fig. 4 the PSNR and SSIM results for both SDMM and ADMM methods for three values of p,

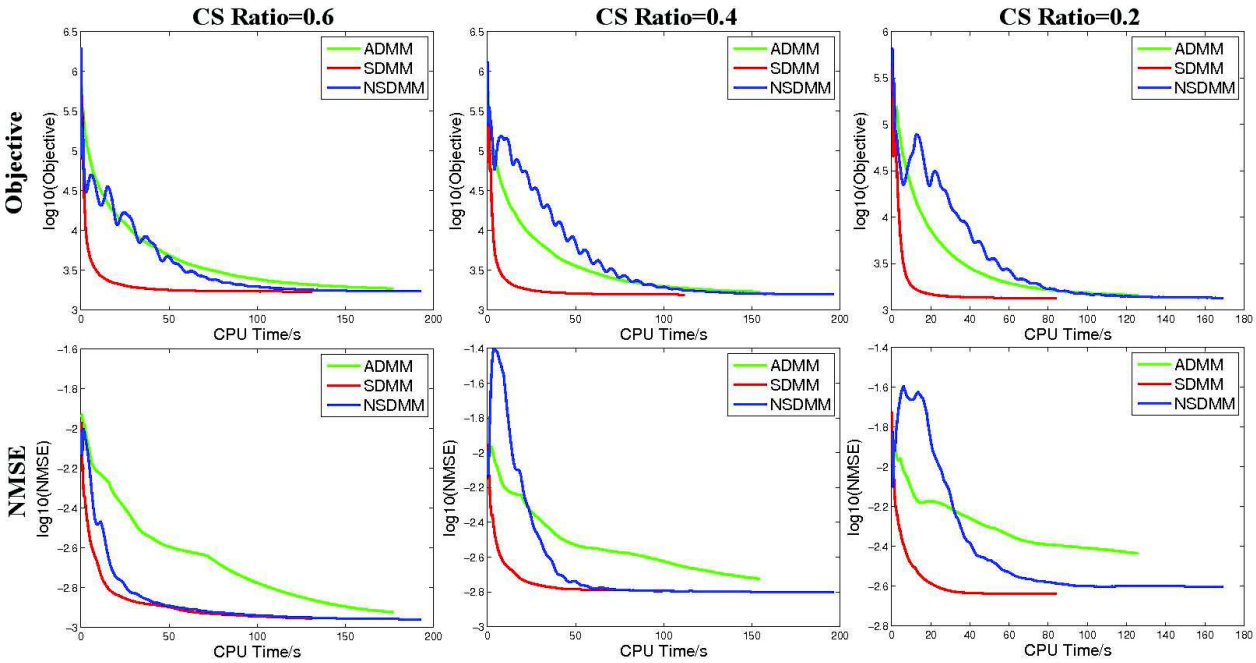

Fig. 3. Convergence performance on simulated data (Group1).

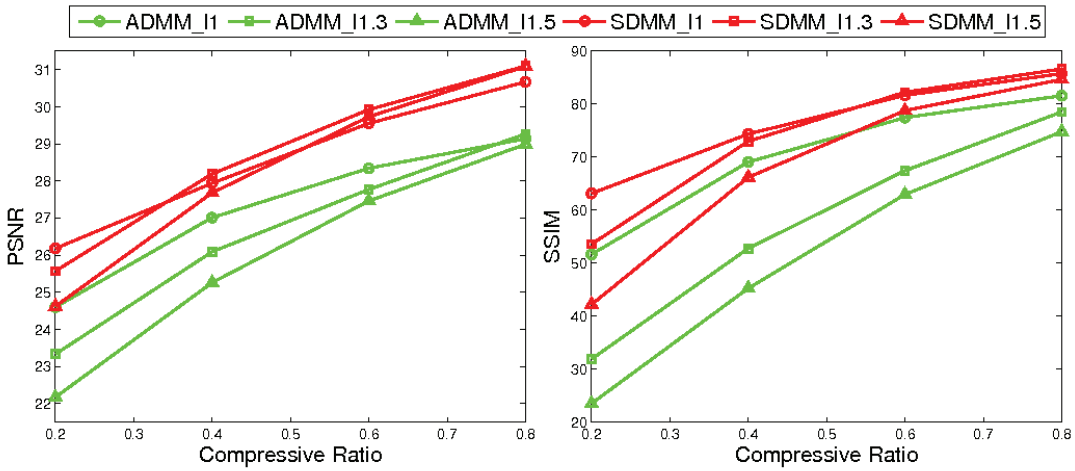

Fig. 4. Results of all the methods with different p on simulated data (Group1).

versus the CS ratio. In addition to the superiority of SDMM compared with ADMM, one may remark that the choice of p is more important for low CS ratios. This observation can be explained by the further importance of the regularization when only a small amount of data is available.

B. Results on In Vivo Data

In this section, we evaluate the results of the proposed SDMM-based CD method on two *in vivo* US images, denoted by Group 3 and Group 4. Group 3 corresponds to a mouse bladder shown in Fig. 5(a), while Group 4 represents a mouse kidney [see Fig. 6(a)]. Both images were acquired with a 20-MHz single-element US probe. Since the PSF is unknown in practical situations, it has been initially estimated from the data, as a preprocessing step, following the PSF estimation procedure presented in [37]. The CD results obtained with ADMM and SDMM are shown in Figs. 5(b)–(g) and 6(b)–(g) for CS ratios of 0.8, 0.6, and 0.4. Given the sparse appearance of the mouse bladder caused by the weak amount of scatterers in the liquid, the value of p was set to 1 for Group 3 and to 1.5 for Group 4.

For the *in vivo* data, the true TRFs are obviously not available, making thus impossible the computation of quantitative results such as the PSNR or the SSIM. As a consequence, the quality of the CD results is evaluated in this section according to the standard contrast-to-noise ratio (CNR) and the resolution gain (RG) proposed in [38]. Moreover, CPU times for both ADMM and SDMM reconstructions are shown in Table II. The CNR values were computed for the regions highlighted by

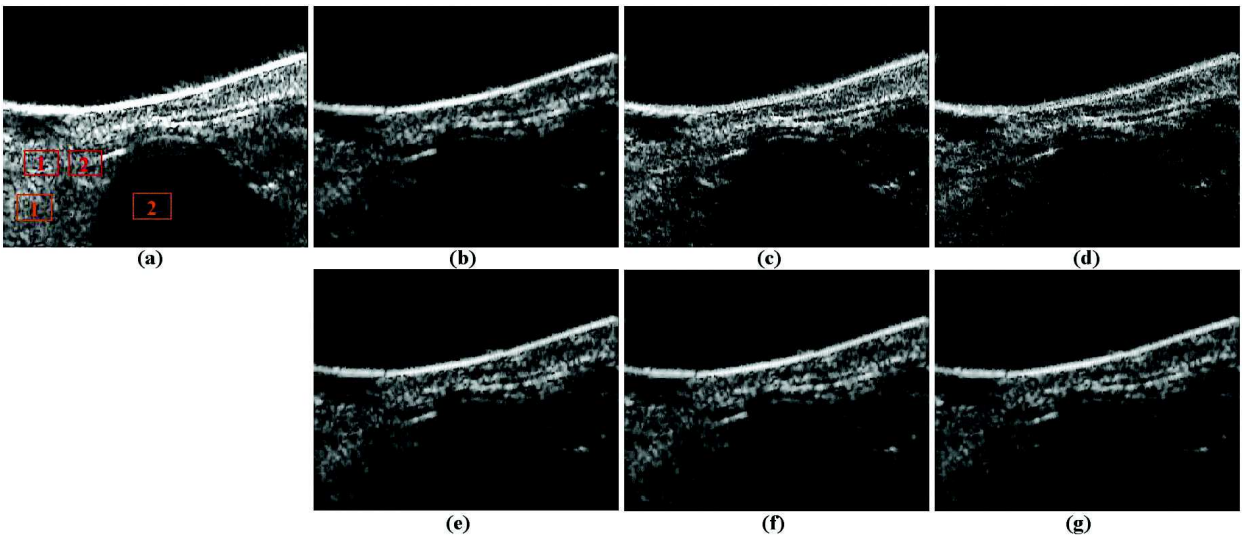

Fig. 5. Results on *in vivo* data (Group 3). (a) Original US image. (b)–(d) Reconstruction results using ADMM for CS ratios of 0.8, 0.6, and 0.4, obtained for $p = 1$. (e)–(g) Reconstruction results using SDMM for CS ratios of 0.8, 0.6, and 0.4, obtained for $p = 1$.

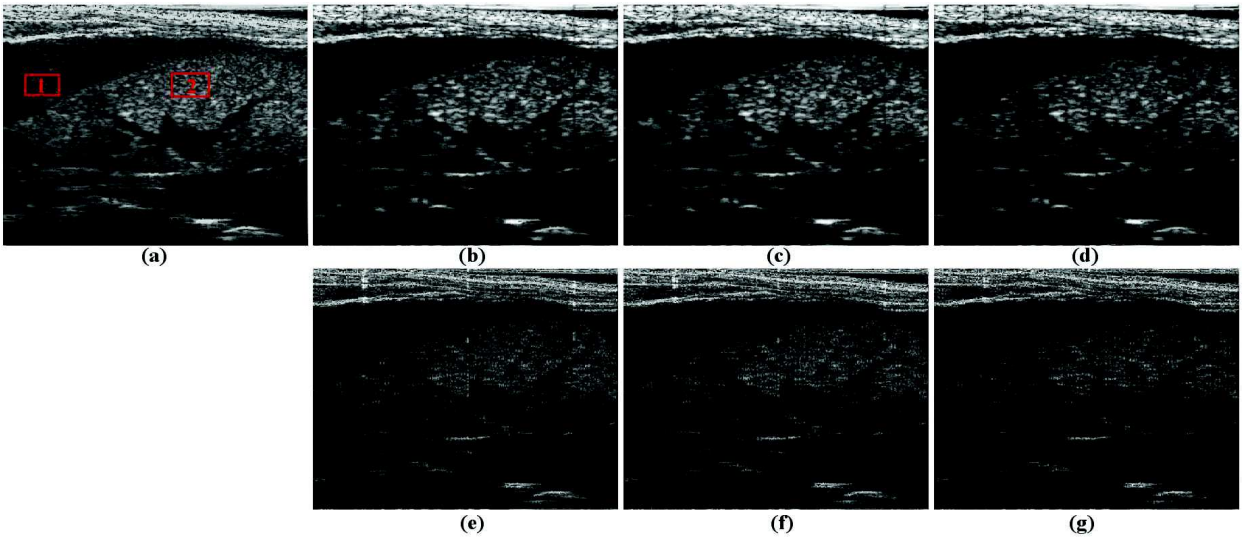

Fig. 6. Results on *in vivo* data (Group 4). (a) Original US image. (b)–(d) Reconstruction results using ADMM for CS ratios of 0.8, 0.6, and 0.4, obtained for $p = 1.5$. (e)–(g) Reconstruction results using SDMM for CS ratios of 0.8, 0.6, and 0.4, obtained for $p = 1.5$.

the red or orange rectangles in Figs. 5 and 6. For instance, two CNRs have been calculated for Group 3, between one region in the bladder cavity and two regions extracted from the bladder wall, respectively. The numbers in Table II, averaged over ten experiments (the results were consistent for each try), show equivalent results between ADMM and SDMM. Nevertheless, SDMM was roughly two to six times faster than ADMM, due to its better convergence properties discussed in the previous section. The contrast of the reconstructed images is shown to be better, in terms of CNR, than the one of the original B-mode images. Moreover, the RG computed between the estimated TRFs and the original images is always larger than 1. This demonstrates the ability of our CD method to improve the spatial resolution.

The visual inspection of the results highlights better denoising achievements with SDMM compared with ADMM, as, for example, in weak scatterer regions such as the bladder cavity.

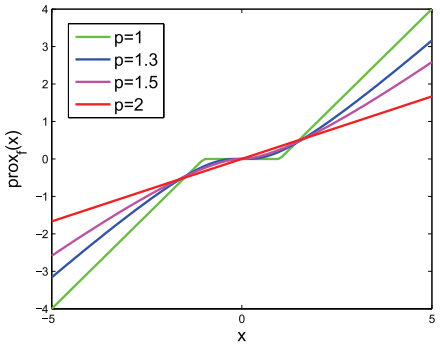

Fig. 7. Proximal operator of $|\ x\ |^p$ for different values of p.

We emphasize that the reconstructed TRF in Figs. 5 and 6 are shown after envelope detection and log compression, in order to be comparable to the standard B-mode images. However, the deconvolution process results in TRFs that, contrary to RF

TABLE II

QUANTITATIVE RESULTS FOR THE *In Vivo* DATA

Images		Group 3				Group 4		
Criterion		CNR1	CNR2	RG	Time/s	CNR	RG	Time/s
Original		1.41	2.62	1.00	-	1.48	1.00	-
ADMM	1	**1.65**	2.51	2.32	76.40	**1.98**	2.69	629.57
	0.8	**1.63**	2.00	2.39	77.36	**1.90**	2.68	561.20
	0.6	**1.57**	1.52	2.45	100.88	1.77	2.34	484.93
	0.4	1.40	1.10	2.50	112.96	1.40	2.68	343.09
SDMM	1	1.61	**2.56**	**3.30**	**12.90**	1.90	**3.50**	**186.64**
	0.8	1.60	**3.28**	**2.39**	**17.62**	1.87	**3.61**	**216.66**
	0.6	1.54	**2.62**	**2.81**	**24.89**	**1.84**	**3.89**	**265.43**
	0.4	**1.52**	**2.07**	**3.17**	**40.57**	**1.58**	**4.17**	**312.12**

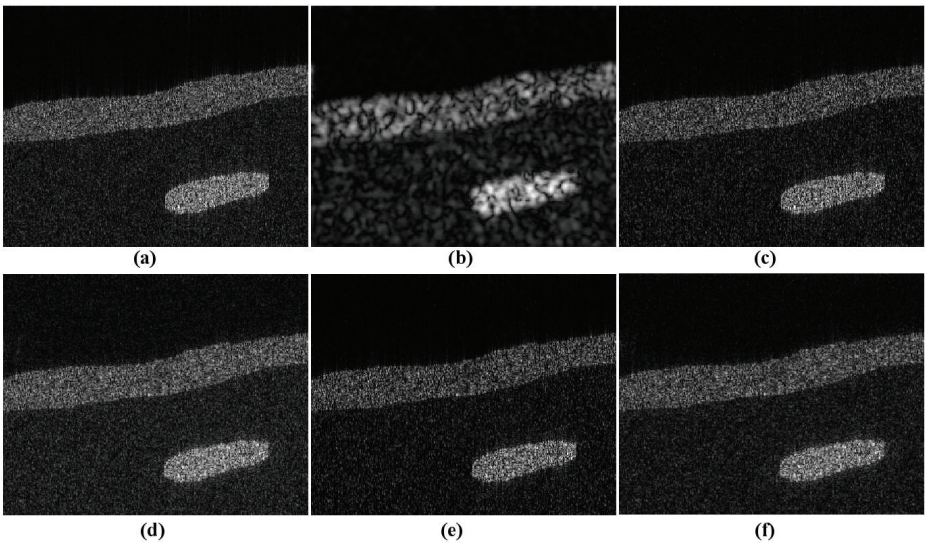

Fig. 8. Results on simulated data (Group 1). (a) TRF. (b) Simulated US image. (c) SDMM. (d) Wiener filtering. (e) Yall1. (f) EM.

images, are not longer modulated in the axial direction. Indeed, the carrier information is included in the PSF that is eliminated during the deconvolution process. For this reason, the standard procedure of envelope detection based on the amplitude of the complex analytic signal is not adapted to the TRF. Instead, we have used an envelope estimator based on the detection and interpolation of local maximum, classically used in empirical mode decomposition techniques [39].

V. CONCLUSION

Reconstructing enhanced US images from compressed measurements is a very recent paradigm that regroups CS and deconvolution into a sole framework. The main objective of this paper was to propose an SDMM-based algorithm dedicated to solve the CD problem in US imaging. Compared with an ADMM-based method that we have recently published in [13], the proposed algorithm requires one less hyperparameter since one of the optimization subproblems can be solved without any approximation. Moreover, the proposed variable splitting scheme made possible by SDMM is shown to allow faster convergence compared with ADMM. Finally, an alternative to compressed measurements obtained with nonorthogonal matrices is provided, thus extending the practical interest of the CD approach. Our future work will include the consideration of blind deconvolution techniques able to jointly estimate the PSF and TRF, through statistical regularization techniques or parametric models. Moreover, an automatic choice of the optimal value of the regularization parameter p would be of great interest in practice. This optimal choice may be considered through statistical assumptions on the US images, such as the heavy-tailed distributions discussed in [22]. While in this paper we focused on p values larger than or equal to 1, the case $p < 1$ may be of interest in practical situations involving sparse US images. To handle both situations, we will mainly focus on an automatic selection of p embedded into both convex and nonconvex optimization routines. Finally, we will consider evaluating our reconstruction method with other existing setups for generating the compressed measurements, having a practical interest in decreasing the acquisition time. As an example, an interesting future research track will be to evaluate the CD with specific compressed measurements, such as those obtained by Xampling [4] or with optimized sparse arrays [40].

APPENDIX A
PROXIMAL OPERATOR

The proximal operator (or proximal mapping) of a function f, denoted by prox_f, is defined by

$$\text{prox}_f(x) = \underset{u\in\mathbb{R}^N}{\text{argmin}} f(u) + \frac{1}{2}\|u - x\|_2^2. \tag{25}$$

TABLE III
QUANTITATIVE COMPARISON WITH DECONVOLUTION METHODS

Method	Wiener	ℓ_1	EM	SDMM
PSNR	29.87	30.38	29.78	31.38
SSIM	81.56	85.83	82.51	87.90

When $f(u) = K \mid u \mid^p$, (25) becomes

$$\text{prox}_{K|\cdot|^p}(x) = \underset{u}{\text{argmin}}\ K \mid u \mid^p + \frac{1}{2}\|u - x\|_2^2 \tag{26}$$

or

$$\text{prox}_{K|\cdot|^p}(x) = \underset{u}{\text{argmin}} \mid u \mid^p + \frac{1}{2K}\|u - x\|_2^2. \tag{27}$$

The unique solution to the above minimization problem given by [29] is

$$\text{prox}_{K|\cdot|^p}(x) = \text{sign}(x)q \tag{28}$$

where $q \geq 0$ and

$$q + pKq^{p-1} = \mid x \mid . \tag{29}$$

For the case $p = 1$, the proximal operator of $K \mid x \mid$ is the well-known thresholding. For the case $p \neq 1$, the numerical solution to the above equation, i.e., the value of q, can be obtained using Newton's method. The resulting proximal operators for different values of p are plotted in Fig. 7.

APPENDIX B
COMPARISON WITH CLASSICAL DECONVOLUTION METHODS

Our reconstruction framework can be used as a deconvolution method if the full data is considered, i.e., without randomly decreasing the number of measurements. In this case, the results can be compared with the ones provided by existing deconvolution techniques. We considered herein, for comparison purpose, three deconvolution methods: the Wiener filter, the ℓ_1-norm constrained optimization solution obtained by Yall1 [41], and the expectation maximization (EM) algorithm in [42]. For the last two methods, the same stopping criterion as the one used for the proposed method has been employed. The experiments were conducted on the simulated image named Group 1 shown in Fig. 1. Fig. 8 regroups the deconvolution results of the proposed SDMM method, for p equal to 1, and the three comparative methods. The corresponding quantitative results reported in Table III show the superiority of the proposed method over the three other deconvolution techniques. While the use of the ℓ_1-norm may explain the superiority over the Wiener filter, based on ℓ_2-norm regularization, our method performs better than EM and ℓ_1 due to the additional regularization term expressed in (2) Thus, the proposed SDMM method can also find an interest in deconvolving US images, in addition to its main objective of recovering enhanced images from compressed measurements.

ACKNOWLEDGMENT

The authors would like to thank Dr. M. Alessandrini for sharing the code of the EM algorithm used for comparison in this paper. The authors would also like to thank Prof. J.-C. Pesquet at Université Paris-Est for his constructive suggestions.

REFERENCES

[1] Z. Chen, A. Basarab, and D. Kouamé, "Joint compressive sampling and deconvolution in ultrasound medical imaging," in *Proc. IEEE Int. Ultrason. Symp. (IUS)*, Oct. 2015, pp. 1–4.

[2] A. Achim, B. Buxton, G. Tzagkarakis, and P. Tsakalides, "Compressive sensing for ultrasound RF echoes using a-stable distributions," in *Proc. Annu. Int. Conf. IEEE Eng. Med. Biol. Soc. (EMBC)*, Aug./Sep. 2010, pp. 4304–4307.

[3] C. Quinsac, A. Basarab, and D. Kouamé, "Frequency domain compressive sampling for ultrasound imaging," *Adv. Acoust. Vibrat.*, vol. 2012, Apr. 2012, Art. no. 231317. [Online]. Available: http://dx.doi.org/10.1155/2012/231317

[4] T. Chernyakova and Y. C. Eldar, "Fourier-domain beamforming: The path to compressed ultrasound imaging," *IEEE Trans. Ultrason., Ferroelectr., Freq. Control*, vol. 61, no. 8, pp. 1252–1267, Aug. 2014.

[5] H. Liebgott, A. Basarab, D. Kouamé, O. Bernard, and D. Friboulet, "Compressive sensing in medical ultrasound," in *Proc. IEEE Int. Ultrason. Symp. (IUS)*, Oct. 2012, pp. 1–6.

[6] H. Liebgott, R. Prost, and D. Friboulet, "Pre-beamformed RF signal reconstruction in medical ultrasound using compressive sensing," *Ultrasonics*, vol. 53, no. 2, pp. 525–533, 2013.

[7] M. F. Schiffner and G. Schmitz, "Pulse-echo ultrasound imaging combining compressed sensing and the fast multipole method," in *Proc. IEEE Int. Ultrason. Symp. (IUS)*, Sep. 2014, pp. 2205–2208.

[8] G. David, J.-L. Robert, B. Zhang, and A. F. Laine, "Time domain compressive beam forming of ultrasound signals," *J. Acoust. Soc. Amer.*, vol. 137, no. 5, pp. 2773–2784, 2015.

[9] O. Lorintiu, H. Liebgott, M. Alessandrini, O. Bernard, and D. Friboulet, "Compressed sensing reconstruction of 3D ultrasound data using dictionary learning and line-wise subsampling," *IEEE Trans. Med. Imag.*, vol. 34, no. 12, pp. 2467–2477, Dec. 2015.

[10] J. Richy, D. Friboulet, A. Bernard, O. Bernard, and H. Liebgott, "Blood velocity estimation using compressive sensing," *IEEE Trans. Med. Imag.*, vol. 32, no. 11, pp. 1979–1988, Nov. 2013.

[11] D. L. Donoho, "Compressed sensing," *IEEE Trans. Inf. Theory*, vol. 52, no. 4, pp. 1289–1306, Apr. 2006.

[12] E. J. Candès, J. Romberg, and T. Tao, "Robust uncertainty principles: Exact signal reconstruction from highly incomplete frequency information," *IEEE Trans. Inf. Theory*, vol. 52, no. 2, pp. 489–509, Feb. 2006.

[13] Z. Chen, A. Basarab, and D. Kouamé, "Compressive deconvolution in medical ultrasound imaging," *IEEE Trans. Med. Imag.*, vol. 35, no. 3, pp. 728–737, Mar. 2016.

[14] J. Ma and F.-X. Le Dimet, "Deblurring from highly incomplete measurements for remote sensing," *IEEE Trans. Geosci. Remote Sens.*, vol. 47, no. 3, pp. 792–802, Mar. 2009.

[15] L. Xiao, J. Shao, L. Huang, and Z. Wei, "Compounded regularization and fast algorithm for compressive sensing deconvolution," in *Proc. IEEE 6th Int. Conf. Image Graph. (ICIG)*, Aug. 2011, pp. 616–621.

[16] M. Zhao and V. Saligrama, "On compressed blind de-convolution of filtered sparse processes," in *Proc. IEEE Int. Conf. Acoust. Speech Signal Process. (ICASSP)*, Mar. 2010, pp. 4038–4041.

[17] B. Amizic, L. Spinoulas, R. Molina, and A. K. Katsaggelos, "Compressive blind image deconvolution," *IEEE Trans. Image Process.*, vol. 22, no. 10, pp. 3994–4006, Oct. 2013.

[18] L. Spinoulas, B. Amizic, M. Vega, R. Molina, and A. K. Katsaggelos, "Simultaneous Bayesian compressive sensing and blind deconvolution," in *Proc. IEEE 20th Eur. Signal Process. Conf. (EUSIPCO)*, Aug. 2012, pp. 1414–1418.

[19] S. Bahmani and J. Romberg, "Compressive deconvolution in random mask imaging," *IEEE Trans. Comput. Imag.*, vol. 1, no. 4, pp. 236–246, Dec. 2015.

[20] M. Alessandrini *et al.*, "A restoration framework for ultrasonic tissue characterization," *IEEE Trans. Ultrason., Ferroelectr., Freq. Controls*, vol. 58, no. 11, pp. 2344–2360, Nov. 2011.

[21] N. Zhao, A. Basarab, D. Kouamé, and J.-Y. Tourneret, "Restoration of ultrasound images using a hierarchical Bayesian model with a generalized Gaussian prior," in *Proc. Int. Conf. Image Process. (ICIP)*, Paris, France, Oct. 2014, pp. 4577–4581.

[22] A. Achim, A. Basarab, G. Tzagkarakis, P. Tsakalides, and D. Kouamé, "Reconstruction of ultrasound RF echoes modeled as stable random variables," *IEEE Trans. Comput. Imag.*, vol. 1, no. 2, pp. 86–95, Jun. 2015.
[23] S. Boyd, N. Parikh, E. Chu, B. Peleato, and J. Eckstein, "Distributed optimization and statistical learning via the alternating direction method of multipliers," *Found. Trends Mach. Learn.*, vol. 3, no. 1, pp. 1–122, Jan. 2011. [Online]. Available: http://dx.doi.org/10.1561/2200000016
[24] S. Setzer, G. Steidl, and T. Teuber, "Deblurring Poissonian images by split Bregman techniques," *J. Vis. Commun. Image Represent.*, vol. 21, no. 3, pp. 193–199, 2010.
[25] T. Goldstein and S. Osher, "The split Bregman method for L1-regularized problems," *SIAM J. Imag. Sci.*, vol. 2, no. 2, pp. 323–343, 2009.
[26] E. Esser, "Applications of Lagrangian-based alternating direction methods and connections to split Bregman," *CAM Rep.*, vol. 9, p. 31, Apr. 2009.
[27] M. K. Ng, P. Weiss, and X. Yuan, "Solving constrained total-variation image restoration and reconstruction problems via alternating direction methods," *SIAM J. Sci. Comput.*, vol. 32, no. 5, pp. 2710–2736, 2010.
[28] J.-C. Pesquet and N. Pustelnik, "A parallel inertial proximal optimization method," *Pacific J. Optim.*, vol. 8, no. 2, pp. 273–305, 2012.
[29] N. Pustelnik, C. Chaux, and J. Pesquet, "Parallel proximal algorithm for image restoration using hybrid regularization," *IEEE Trans. Image Process.*, vol. 20, no. 9, pp. 2450–2462, Sep. 2011.
[30] N. Pustelnik, J.-C. Pesquet, and C. Chaux, "Relaxing tight frame condition in parallel proximal methods for signal restoration," *IEEE Trans. Signal Process.*, vol. 60, no. 2, pp. 968–973, Feb. 2012.
[31] P. L. Combettes and J.-C. Pesquet, "Proximal splitting methods in signal processing," in *Fixed-Point Algorithms for Inverse Problems in Science and Engineering*. New York, NY, USA: Springer, 2011, pp. 185–212.
[32] Z. Chen, N. Zhao, A. Basarab, and D. Kouamé, "Ultrasound compressive deconvolution with ℓ_p-norm prior," in *Proc. IEEE 23rd Eur. Signal Process. Conf. (EUSIPCO)*, Aug./Sep. 2015, pp. 2791–2795.
[33] W. Deng, W. Yin, and Y. Zhang, "Group sparse optimization by alternating direction method," *Proc. SPIE*, vol. 8858, p. 88580R, Sep. 2013. [Online]. Available: http://dx.doi.org/10.1117/12.2024410
[34] J. Ng, R. Prager, N. Kingsbury, G. Treece, and A. Gee, "Wavelet restoration of medical pulse-echo ultrasound images in an em framework," *IEEE Trans. Ultrason., Ferroelectr., Freq. Control*, vol. 54, no. 3, pp. 550–568, Mar. 2007.
[35] J. A. Jensen, "A model for the propagation and scattering of ultrasound in tissue," *Acoust. Soc. Amer. J.*, vol. 89, no. 1, pp. 182–190, 1991.
[36] T. T. Do, L. Gan, N. H. Nguyen, and T. D. Tran, "Fast and efficient compressive sensing using structurally random matrices," *IEEE Trans. Signal Process.*, vol. 60, no. 1, pp. 139–154, Jan. 2012.
[37] O. V. Michailovich and D. Adam, "A novel approach to the 2-D blind deconvolution problem in medical ultrasound," *IEEE Trans. Med. Imag.*, vol. 24, no. 1, pp. 86–104, Jan. 2005.
[38] C. Yu, C. Zhang, and L. Xie, "A blind deconvolution approach to ultrasound imaging," *IEEE Trans. Ultrason., Ferroelectr., Freq. Control*, vol. 59, no. 2, pp. 271–280, Feb. 2012.
[39] P. Flandrin, G. Rilling, and P. Goncalves, "Empirical mode decomposition as a filter bank," *IEEE Signal Process. Lett.*, vol. 11, no. 2, pp. 112–114, Feb. 2004.
[40] B. Diarra, M. Robini, P. Tortoli, C. Cachard, and H. Liebgott, "Design of optimal 2-D nongrid sparse arrays for medical ultrasound," *IEEE Trans. Biomed. Eng.*, vol. 60, no. 11, pp. 3093–3102, Nov. 2013.
[41] J. Yang and Y. Zhang, "Alternating direction algorithms for ℓ_1-problems in compressive sensing," *SIAM J. Sci. Comput.*, vol. 33, no. 1, pp. 250–278, 2011.
[42] M. Alessandrini, A. Palladini, L. De Marchi, and N. Speciale, "Expectation maximization for joint deconvolution and statistics estimation," in *Acoustical Imaging*. The Netherlands: Springer, 2011, pp. 335–343.

Zhouye Chen (S'14) received the B.Sc. degree in electrical engineering from the Dalian University of Technology, Dalian, China, in 2010, and the M.Sc. degree from the University of Chinese Academy of Sciences, Beijing, China, in 2013. She is currently pursuing the Ph.D. degree with the Paul Sabatier University of Toulouse III, Toulouse, France, and the Centre National de la Recherche Scientifique, Institut de Recherche en Informatique de Toulouse, University of Toulouse, Toulouse.

Her current research interests include inverse problems of image processing, in particular, deconvolution and compressive sampling.

Ms. Chen's paper "Joint Compressive Sampling and Deconvolution in Ultrasound Medical Imaging" was selected as one of the best student paper finalists at the IEEE International Ultrasonics Symposium in 2015.

Adrian Basarab (S'05–M'08) received the M.S. and Ph.D. degrees in signal and image processing from the National Institute for Applied Sciences of Lyon, Lyon, France, in 2005 and 2008, respectively.

He has been an Assistant Professor with the Paul Sabatier University of Toulouse III, Toulouse, France, and a member of the Centre National de la Recherche Scientifique with the Institut de Recherche en Informatique de Toulouse, University of Toulouse, Toulouse, since 2009. His current research interests include medical imaging, and in particular, motion estimation, inverse problems, and ultrasound image formation.

Dr. Basarab is currently an Associate Editor of *Digital Signal Processing*.

Denis Kouamé (M'97) received the Ph.D. and H.D.R. degrees in signal processing and medical ultrasound imaging from the University of Tours, Tours, France, in 1996 and 2004, respectively.

He was a Senior Engineer with GIP Tours, Tours, from 1996 to 1998. From 1998 to 2008, he was an Assistant and then an Associate Professor with the University of Tours. He was the head of the Signal and Image Processing Group from 2000 to 2006, and then the Head of the Ultrasound Imaging Group with the Ultrasound and Signal Laboratory, University of Tours, from 2006 to 2008. He is currently a Professor with the Paul Sabatier University of Toulouse III, Toulouse, France, and a member of the Centre National de la Recherche Scientifique with the Institut de Recherche en Informatique de Toulouse, University of Toulouse, Toulouse, where he currently leads the Image Comprehension and Processing Group. His current research interests include signal and image processing with applications to medical imaging, and in particular, ultrasound imaging, including high-resolution imaging, image resolution enhancement, Doppler signal processing, detection and estimation with application to cerebral emboli detection, multidimensional parametric modeling, spectral analysis, and inverse problems related to compressed sensing and restoration.

Dr. Kouamé has been serving as an Associate Editor of the IEEE TRANSACTIONS ON ULTRASONICS, FERROELECTRICS, AND FREQUENCY CONTROL. He has been involved in the organization of several conferences. He has also led a number of invited conferences, special sessions, and tutorials in this area at several IEEE conferences and workshops.